Discovery and Preliminary Characterization of a Third Interstellar Object: 3I/ATLAS

Darryl Z. Seligman[1,33] , Marco Micheli[2] , Davide Farnocchia[3] , Larry Denneau[4] , John W. Noonan[5] , Henry H. Hsieh[6] ,
Toni Santana-Ros[7,8] , John Tonry[4] , Katie Auchettl[9,10] , Luca Conversi[2] , Maxime Devogèle[2] , Laura Faggioli[2] ,
Adina D. Feinstein[1,34] , Marco Fenucci[2] , Marin Ferrais[11] , Tessa Frincke[1] , Michael Gillon[12] , Olivier R. Hainaut[13] ,
Kyle Hart[4] , Andrew Hoffman[4] , Carrie E. Holt[14] , Willem B. Hoogendam[4,35] , Mark E. Huber[4] , Emmanuel Jehin[15] ,
Theodore Kareta[16,17] , Jacqueline V. Keane[18] , Michael S. P. Kelley[19] , Tim Lister[14] , Kathleen Mandt[20] ,
Jean Manfroid[15] , Dušan Marčeta[21] , Karen J. Meech[4] , Mohamed Amine Miftah[15,22] , Marvin Morgan[23] ,
Francisco Ocaña[2] , Eloy Peña-Asensio[24] , Benjamin J. Shappee[4] , Robert J. Siverd[4] , Aster G. Taylor[25,36] ,
Michael A. Tucker[26,27] , Richard Wainscoat[4] , Robert Weryk[28] , James J. Wray[29] , Atsuhiro Yaginuma[30] , Bin Yang[31] ,
Quanzhi Ye (叶泉志)[19,32] , and Qicheng Zhang[17]
[1] Department of Physics and Astronomy, Michigan State University, East Lansing, MI 48824, USA; dzs@msu.edu
[2] ESA NEO Coordination Centre, Largo Galileo Galilei 1, I-00044 Frascati (RM), Italy
[3] Jet Propulsion Laboratory, California Institute of Technology, 4800 Oak Grove Dr., Pasadena, CA 91109, USA
[4] Institute for Astronomy, University of Hawaii, 2680 Woodlawn Drive, Honolulu, HI 96822, USA
[5] Department of Physics, Auburn University, Edmund C. Leach Science Center, Auburn, AL 36849, USA
[6] Planetary Science Institute, 1700 East Fort Lowell Rd., Suite 106, Tucson, AZ 85719, USA
[7] Departamento de Física, Ingeniería de Sistemas y Teoría de la Señal, Universidad de Alicante, Carr. San Vicente del Raspeig, s/n, 03690 San Vicente del Raspeig,
Alicante, Spain
[8] Institut de Ciències del Cosmos (ICCUB), Universitat de Barcelona (UB), c. Martí Franquès, 1, 08028 Barcelona, Catalonia, Spain
[9] School of Physics, University of Melbourne, Parkville, VIC 3010, Australia
[10] Department of Astronomy and Astrophysics, University of California, Santa Cruz, CA 93105, USA
[11] Florida Space Institute, University of Central Florida, 12354 Research Parkway, Orlando, FL 32828, USA
[12] Astrobiology Research Unit, Université de Liège, 4000 Liège, Belgium
[13] European Southern Observatory, Karl-Schwarzschild-St. 2, 85748 Garching-bei-München, Germany
[14] Las Cumbres Observatory, 6740 Cortona Drive, Suite 102, Goleta, CA 93117, USA
[15] Space sciences, Technologies & Astrophysics Research (STAR) Institute Université de Liége 4000 Liege, Belgium
[16] Dept. of Astrophysics and Planetary Science, Villanova University, Villanova, PA, USA
[17] Lowell Observatory, 1400 W Mars Hill Rd, Flagstaff, AZ 86001, USA
[18] U.S. National Science Foundation, 2415 Eisenhower Avenue, Alexandria, VA 22314, USA
[19] Department of Astronomy, University of Maryland, College Park, MD 20742-0001, USA
[20] NASA Goddard Space Flight Center, Greenbelt, MD 20771, USA
[21] Department of Astronomy, Faculty of Mathematics, University of Belgrade, Serbia
[22] Cadi Ayyad University (UCA), Oukaimeden Observatory (OUCA), Faculté des Sciences Semlalia (FSSM), High Energy Physics, Astrophysics and Geoscience
Laboratory (LPHEAG), Marrakech, Morocco
[23] Department of Physics, University of California, Santa Barbara, Santa Barbara, CA 93106, USA
[24] Department of Aerospace Science and Technology, Politecnico di Milano, Via La Masa 34, 20156 Milano, Italy
[25] Dept. of Astronomy, University of Michigan, Ann Arbor, MI 48109, USA
[26] Center for Cosmology & Astroparticle Physics, The Ohio State University, Columbus, OH, USA
[27] Department of Astronomy, The Ohio State University, Columbus, OH, USA
[28] Department of Physics and Astronomy, The University of Western Ontario, 1151 Richmond Street, London, ON N6A 3K7, Canada
[29] School of Earth and Atmospheric Sciences, Georgia Institute of Technology, 311 Ferst Drive, Atlanta, GA 30332, USA
[30] Dept. of Physics and Astronomy, Michigan State University, East Lansing, MI 48824, USA
[31] Instituto de Estudios Astrofísicos, Facultad de Ingeniería y Ciencias, Universidad Diego Portales, Santiago, Chile
[32] Center for Space Physics, Boston University, 725 Commonwealth Ave, Boston, MA 02215, USA

Abstract

We report initial observations aimed at the characterization of a third interstellar object. This object, 3I/ATLAS or C/2025 N1 (ATLAS), was discovered on 2025 July 1 UT and has an orbital eccentricity of $e \sim 6.1$, perihelion of $q \sim 1.36$ au, inclination of $\sim 175°$, and hyperbolic velocity of $V_\infty \sim 58$ km s^{-1}. We report deep stacked images obtained using the Canada–France–Hawaii Telescope and the Very Large Telescope that resolve a compact coma. Using images obtained from several smaller ground-based telescopes, we find minimal light-curve variation for the object over a ~ 4 day time span. The visible/near-infrared spectral slope of the object is $17.1\% \pm 0.2\%/$ 100 nm, comparable to other interstellar objects and primitive solar system small bodies (comets and D-type asteroids). Moreover, 3I/ATLAS will be observable through early 2025 September, then unobservable by Earth-

based observatories near perihelion due to low solar elongation. It will be observable again from the ground in late 2025 November. Although this limitation unfortunately prohibits detailed Earth-based observations at perihelion when the activity of 3I/ATLAS is likely to peak, spacecraft at Mars could be used to make valuable observations at this time.

Unified Astronomy Thesaurus concepts: Interstellar objects (52); Asteroids (72); Comets (280); Meteors (1041)

1. Introduction

The first two interstellar objects identified traversing the inner solar system, 1I/'Oumuamua (G. V. Williams et al. 2017) and 2I/Borisov (G. Borisov et al. 2019), were discovered in 2017 and 2019, respectively. It has been suggested that interstellar objects formed in protostellar disks (A. Fitzsimmons et al. 2024) or the cores of giant molecular clouds (C.-H. Hsieh et al. 2021). Although there is little hope of identifying the exact home system for a given interstellar object (T. Hallatt & P. Wiegert 2020), they provide the best opportunity to directly measure the properties of small bodies that formed outside of our solar system.

These first interstellar objects displayed divergent properties. For one, 1I/'Oumuamua displayed no visible activity (D. Jewitt et al. 2017; K. J. Meech et al. 2017; Q.-Z. Ye et al. 2017; D. E. Trilling et al. 2018), yet nongravitational acceleration was detected in its trajectory at the $\sim 30\sigma$ level (M. Micheli et al. 2018). Meanwhile, 2I/Borisov displayed clear outgassing and dust ejection activity (A. Fitzsimmons et al. 2019; D. Jewitt & J. Luu 2019; G. Cremonese et al. 2020; P. Guzik et al. 2020; M.-T. Hui et al. 2020; Y. Kim et al. 2020; A. J. McKay et al. 2020; Q. Ye et al. 2020; B. Yang et al. 2021). The excess velocity of 1I/'Oumuamua and 2I/Borisov also differed significantly. These objects had velocities of $V_\infty \sim 26$ and $V_\infty \sim 32$ km s^{-1} respectively, which approximately correspond to ages of $\sim 10^2$ and $\sim 10^3$ Myr (E. Gaidos et al. 2017; E. Mamajek 2017; F. Feng & H. R. A. Jones 2018; F. Almeida-Fernandes & H. J. Rocha-Pinto 2018; T. Hallatt & P. Wiegert 2020; C.-H. Hsieh et al. 2021). In addition, 1I/'Oumuamua displayed brightness variations of ~ 3.5 mag corresponding to an extreme oblate 6:6:1 geometry (M. M. Knight et al. 2017; K. J. Meech et al. 2017; M. J. S. Belton et al. 2018; ; W. C. Fraser et al. 2018; S. Mashchenko 2019; A. G. Taylor et al. 2023) and had a moderately red reflectance spectrum (K. J. Meech et al. 2017; Q.-Z. Ye et al. 2017; A. Fitzsimmons et al. 2018).

These divergent properties led to a variety of hypotheses regarding the provenance of the population. Although 2I/Borisov's coma was found to contain volatile species typically seen in comets (C. Opitom et al. 2019; M. T. Bannister et al. 2020; T. Kareta et al. 2020; H. W. Lin et al. 2020; Z. Xing et al. 2020; K. Aravind et al. 2021; S. Bagnulo et al. 2021), it had a high enrichment of CO relative to H_2O (D. Bodewits et al. 2020; M. A. Cordiner et al. 2020). These ratios differentiate its composition from most solar system comets, which are typically rich in H_2O and contain CO between 1% and 15% relative to water (N. Biver et al. 2024).

Moreover, 1I/'Oumuamua's lack of visible activity despite its nongravitational acceleration has led to a variety of hypothesized origins. M. Micheli et al. (2018) noted that for radiation pressure to cause the nongravitational acceleration, the object must either have an exceptionally low density or an extreme geometry. Such a density is a possible byproduct of diffusion-limited aggregation formation processes in the outskirts of a protostellar disk (A. Moro-Martín 2019).

Somewhat counterintuitively, it has also been demonstrated that such hypothetical structures bound together by weak van der Waals forces could survive tidal disruption from the solar gravity (E. G. Flekkøy et al. 2019). It was also hypothesized that such a fractal aggregate could form in the coma of an undiscovered parent interstellar comet (J. X. Luu et al. 2020).

Alternatively, 1I/'Oumuamua could have been outgassing volatiles with low levels of dust production, rendering it photometrically inactive in all extant observations (M. Micheli et al. 2018; Z. Sekanina 2019; D. Seligman & G. Laughlin 2020; S. J. Desch & A. P. Jackson 2021; A. P. Jackson & S. J. Desch 2021; W. G. Levine & G. Laughlin 2021; W. G. Levine et al. 2021; S. J. Desch & A. P. Jackson 2022; J. B. Bergner & D. Z. Seligman 2023). This argument has been recently bolstered; since the discovery of 1I/'Oumuamua, a series of photometrically inactive near-Earth objects (NEOs) have been reported to have significant comet-like nongravitational accelerations (D. Farnocchia et al. 2023; D. Z. Seligman et al. 2023, 2024). These objects imply that 1I/'Oumuamua-like nongravitational accelerations may be more common than previously thought (A. G. Taylor et al. 2024). Regardless, our understanding of interstellar objects is incomplete. See A. Fitzsimmons et al. (2024), D. Z. Seligman & A. Moro-Martín (2023), D. Jewitt & D. Z. Seligman (2023), and A. Moro-Martín (2022) for recent reviews on this topic.

In this Letter, we report early observations of 3I/ATLAS (L. Denneau et al. 2025), the third interstellar object to be discovered after 1I/'Oumuamua and 2I/Borisov, to help inform and coordinate follow-up observations. Preliminary observations of 3I/ATLAS were reported contemporaneously with this Letter (M. R. Alarcon et al. 2025; ; M. Belyakov et al. 2025; R. de la Fuente Marcos et al. 2025; D. Jewitt & J. Luu 2025; T. Kareta et al. 2025; C. Opitom et al. 2025; B. Yang et al. 2025), along with theoretical calculations (A. Hibberd et al. 2025; M. J. Hopkins et al. 2025; A. Loeb 2025; A. G. Taylor & D. Z. Seligman 2025; A. Yaginuma et al. 2025).

2. Discovery and Hyperbolic Orbit Characterization

2.1. Discovery

On 2025 July 1 3I/ATLAS was discovered through the robotic observing schedule from ATLAS Chile (J. L. Tonry et al. 2018a) and given the internal designation A11pl3Z[37] (see Figure 1). The discovery tracklet was immediately submitted to the Minor Planet Center (MPC). Follow-up observations were then conducted by ATLAS in Hawai'i, Sutherland, and the Canary Islands, along with dozens of other observatories worldwide. The discovery was made by ATLAS largely because the object was located in the Galactic plane—a region typically avoided by more sensitive surveys, such as Pan-STARRS and the Catalina Sky Survey.

---

[37] https://www.minorplanetcenter.net/mpec/K25/K25N12.html

Table 1
Initial Orbit of 3I/ATLAS, Computed Using Astrometry from 2025 May 22 to 2025 July 6

Orbital element	Value $\pm 1\sigma$
Perihelion distance q [au]	1.3558541 $\pm$ 0.0019855
Eccentricity e	6.1329072 $\pm$ 0.0162018
Inclination i [°]	175.11239 $\pm$ 0.00089
Longitude of ascending node Ω [°]	322.14485 $\pm$ 0.01806
Argument of perihelion ω [°]	128.01038 $\pm$ 0.02340
Time of perihelion T_P [MJD, TDB]	60977.51085 $\pm$ 0.04078

Note. Heliocentric orbital elements at the epoch of 2025 July 3.

Prediscovery detections from 2025 June 28 to 29 were identified in Zwicky Transient Facility (ZTF; E. C. Bellm et al. 2019; M. J. Graham et al. 2019) survey data 6 hr after the initial detection by ATLAS on 2025 July 1, extending the orbital arc from 3.3 hr to 3 days. The new 3 day arc suggested a strongly hyperbolic orbit and prompted speculation on community mailing lists that the object might be interstellar. Later during the early hours of 2025 July 2 UT, additional prediscovery pairs and triplets were identified in ATLAS data from 5 days earlier and later refined and resubmitted to the MPC by the ATLAS team (L. Denneau et al. 2025). More prediscovery detections from ZTF, dating back to 2025 June 14,[38] were also identified and submitted.

At the time of discovery in the ATLAS data, the object had a magnitude 17.7–17.9 in the o-band filter (see Figure 1) and was at a heliocentric distance of $r = 4.51$ au and a geocentric distance of $\Delta = 3.50$ au.

2.2. Orbit Characterization

As of the early hours of 2025 July 2, the initial discovery and prediscovery arc, covering a total of about 18 days, was sufficient to confirm the large eccentricity and, consequently, hyperbolic nature of the object's orbit. As soon as the unusual nature of the object became evident, a large number of follow-up observations were obtained on 2025 July 2 by various observatories, leading to additional orbit refinement.

We first acquired 31 unfiltered 163 s exposures starting at 06:34 UT on 2025 July 2 spanning a total of 93 minutes using the European Space Agency's (ESA) 0.56 m Test Bed Telescope (TBT; MPC code W57) at La Silla Observatory in Chile, which has a field of view of $2°.5 \times 2°.5$. The telescope is fully devoted to NEO survey and follow-up observations and can be interrupted at any time for high-profile targets.

We also obtained detections with one of the Las Cumbres Observatory (LCO) 0.35 m telescopes on Haleakalā (MPC code T03) and with the 2.0 m Faulkes Telescope North (FTN; MPC code F65) and South (FTS; MPC code E10) between 2025 July 2 and 4, which provided astrometric measurements with an astrometric accuracy better than $\pm 0''.25$.

A successful DDT request to the European Southern Observatory's (ESO) 8.2 m Very Large Telescope (VLT), submitted on the same day and quickly approved, also allowed our team to obtain images of the object during good seeing on 2025 July 4. High-precision astrometry (better than $\pm 0''.1$) was extracted from this data set, using an extrapolation to zero
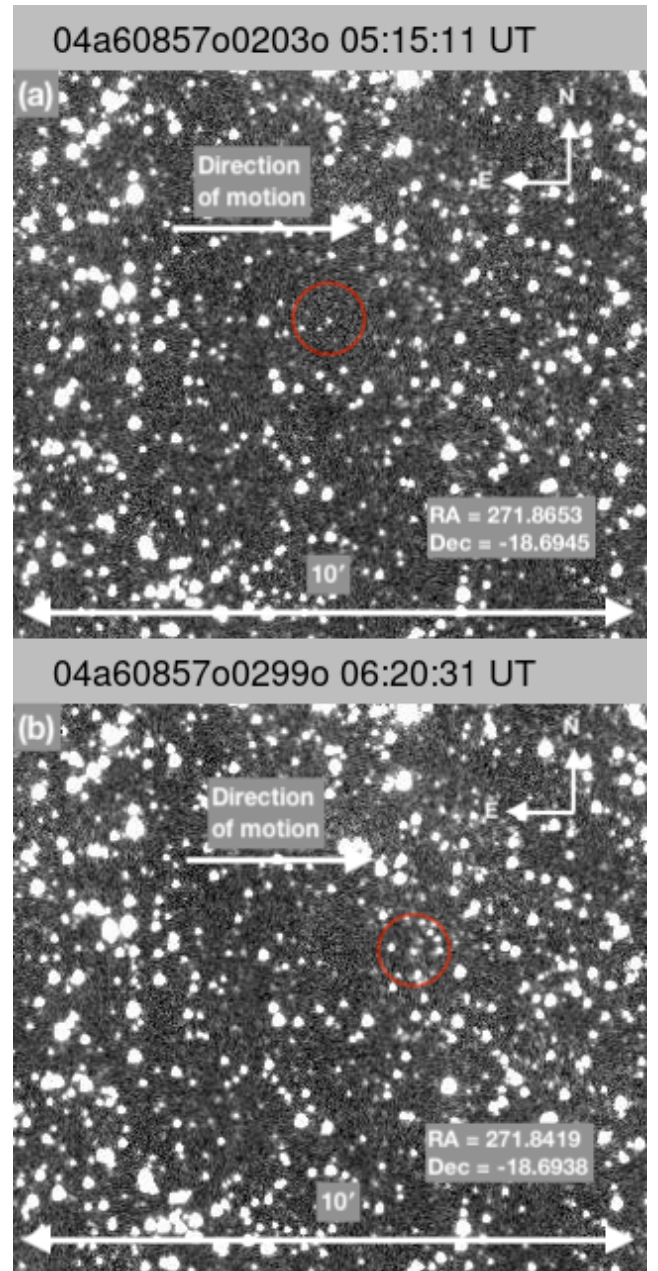
Figure 1. Cutout images from the first and fourth discovery observations of 3I/ATLAS from the ATLAS Chile, spanning approximately 1 hr—3I/ATLAS is moving at 0.49 deg day^{-1} against the stellar background. The cardinal directions and direction of motion are indicated with arrows, and 3I/ATLAS is identified within the red circle. (a) Unbackground subtracted image from 05:15:11 UT; (b) unbackground subtracted image from 06:20:31 UT.

aperture to ensure correction for possible asymmetries in the inner coma of the object. Gaia DR3 (Gaia Collaboration et al. 2023) was used as the reference catalog for the astrometric solutions.

Our best estimate of the heliocentric orbital elements of the object, at the time of submission of this Letter is listed in Table 1. In Figure 2, we show the orbit of 3I/ATLAS in comparison to previously discovered interstellar objects.

From the current heliocentric orbit, it is possible to infer the incoming trajectory of the object before it entered our solar system. The eccentricity of the object's orbit with respect to the solar system barycenter, computed before interacting with

---

[38] Another batch of ZTF prediscovery detections, dating back to 2025 May 22, was later submitted and published in MPEC 2025-N51 (https://minorplanetcenter.net/mpec/K25/K25N51.html).
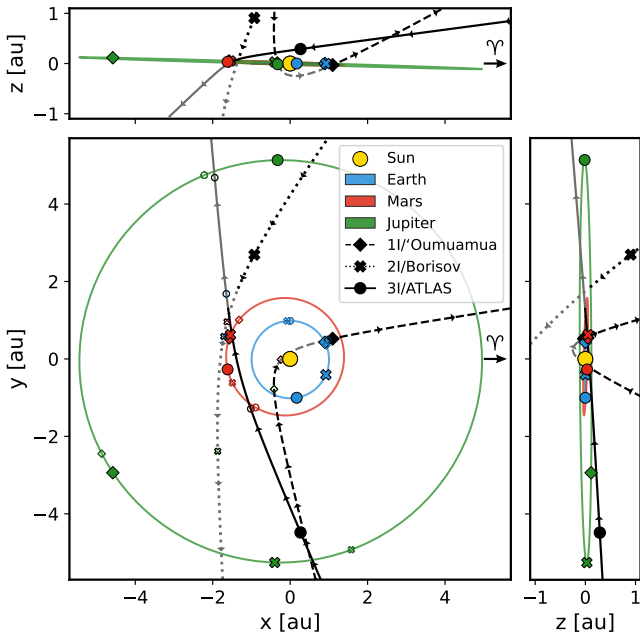
Figure 2. Heliocentric orbit (ECLIPJ2000) of 1I/'Oumuamua, 2I/Borisov, 3I/ATLAS, Earth, Mars, and Jupiter. Black lines represent the orbital path of each object; gray lines represent when the interstellar object is below ecliptic. We highlight the location of the Sun (yellow) and the orbital paths of Earth (blue), Mars (red), and Jupiter (green). Large filled markers represent where the respective colored planet was when the interstellar object was discovered. Small unfilled markers represent where the planet will be at the interstellar object's closest approach. Arrows point along the motion direction. The vernal equinox is indicated to the right.

our planetary system, can be extrapolated as $e_b = 6.144 \pm 0.016$. This value, together with an incoming pericenter distance of $q_b = (1.3611 \pm 0.0020)$ au, results in an incoming velocity $v_\infty = (57.942 \pm 0.049)$ km s^{-1}, from an asymptote directed toward a R.A. of $\sim 295°$ and a decl. of $\sim -19°$, in the constellation of Sagittarius and not far from the Galactic center.

3. Observational Analysis

3.1. Activity

Given the stark difference in visible activity levels between 1I/'Oumuamua and 2I/Borisov (Section 1), a high priority for initial observational analysis for 3I/ATLAS was determining whether it was active or not. With this in mind, we obtained three 60 s nonsidereally guided *gri*-band images with the MegaCam wide-field mosaic imager (O. Boulade et al. 2003) on the 3.6 m Canada–France–Hawaii Telescope (CFHT; MPC code T14) on 2025 July 2 to search for faint cometary activity. The highest-quality image had typical stellar FHWMs of $0\rlap{.}''72 \pm 0\rlap{.}''05$ measured perpendicular to the direction of trailing, while the object had a FWHM of $1\rlap{.}''29 \pm 0\rlap{.}''02$. The magnitude in a $5\rlap{.}''0$ radius aperture was 17.2 in the Gaia DR2 *G band* after three background stars were masked, although the field was crowded, so we consider this measurement to be unreliable. Figure 3(a) shows the stacked composite image of these data in which faint activity is visible.

On 2025 July 4, fifteen 10 s *R*-band images were acquired using the FORS2 instrument on the 8.2 m Unit Telescope 1 of the ESO VLT on Cerro Paranal, Chile. The measured stellar image quality was $0\rlap{.}''6$ FWHM. However, the object had a
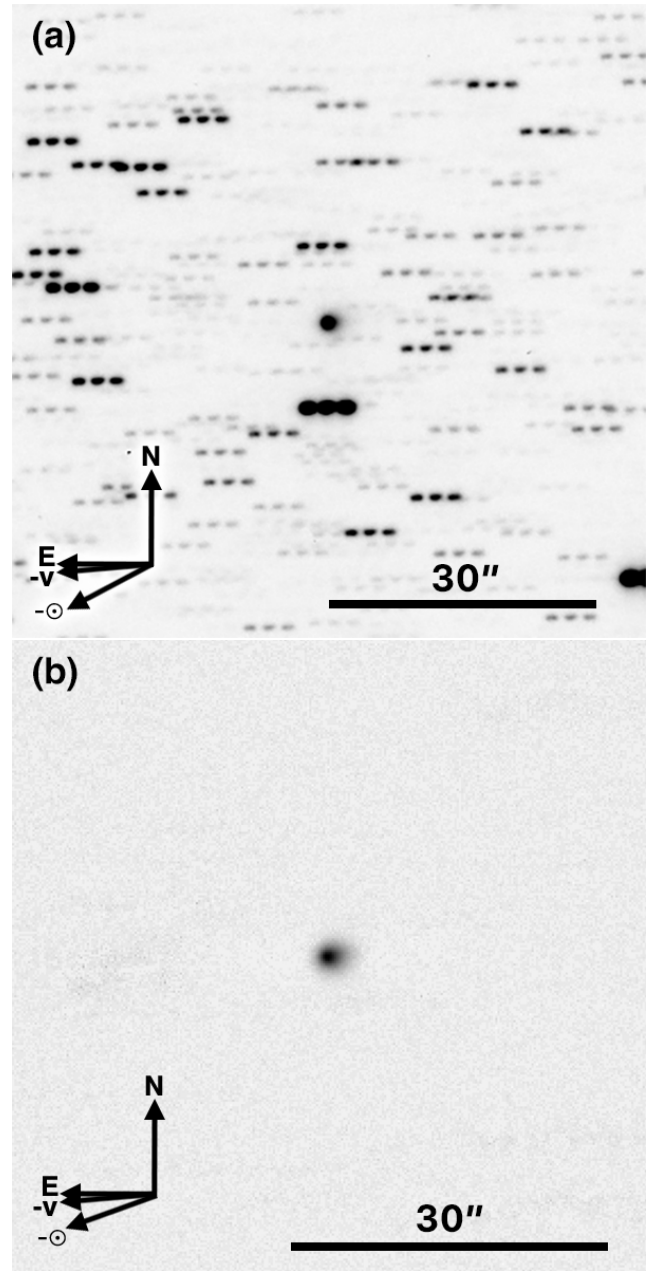
Figure 3. (a) Stacked *gri*-band image cut out from CFHT on 2025 July 2 and (b) *R*-band composite image from VLT on 2025 July 4, both showing faint activity. Background objects were removed from the VLT stack. Arrows indicate the directions of north (N), east (E), the antisolar vector as projected on the sky ($-\odot$) and the negative heliocentric velocity vector as projected on the sky ($-v$).

FWHM of $1\rlap{.}''49 \times 1\rlap{.}''29$ with the asymmetric elongation pointing to position angle 277° from north to east, where the coma can be seen extending out to $3\rlap{.}''5$. A composite image of these data is shown in Figure 3(b). The photometric profile of the object (Figure 4) shows a brightness excess extending over $4\rlap{.}''0$ compared to that of field stars.

As noted in Section 2, *g'*- and *r'*-band precovery data from ZTF were published in MPEC 2025-N51 following these observations. This included photometry dating back to 2025 May 22, all of which were measured from difference images (produced by subtracting an appropriately matched template sky image from the target image) using aperture photometry
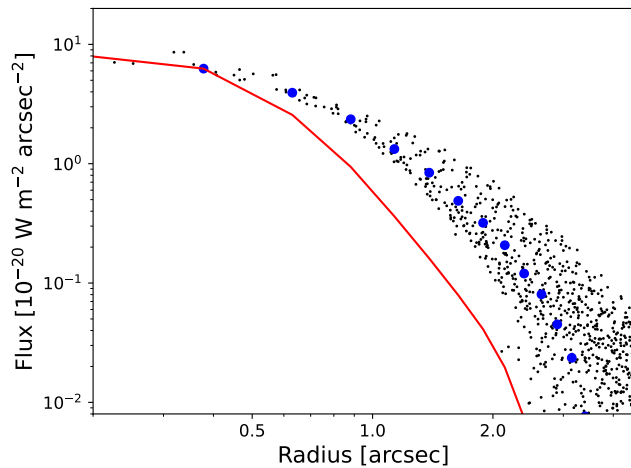
Figure 4. Photometric profile of the VLT image (Figure 3(a)). The individual pixels are represented by black dots; average in annuli by blue circles. The red line is the average stellar profile measured on 10 nearby well-exposed stars.
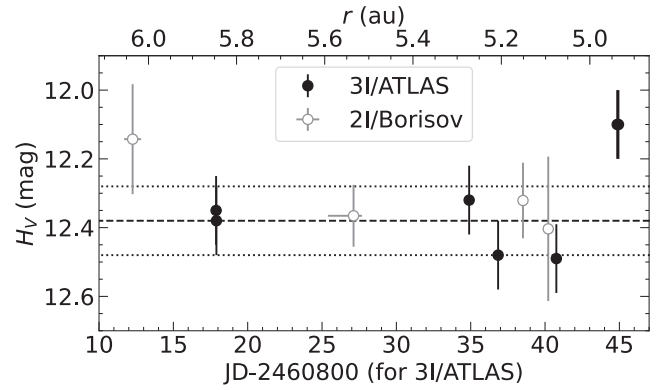

Figure 5. Absolute magnitudes computed from ZTF precovery data published in MPEC 2025-N51 from 2025 May 22 to June 18 (black filled dots). The median H_V and standard deviation of data are shown by a dashed horizontal line and dotted horizontal lines, respectively. No uncertainties were reported for these original data, and so plotted uncertainties are estimated based on the standard deviation of photometric points measured between 2025 May 22 and June 14. Corresponding preperihelion H_V for 2I/Borisov derived from Q. Ye et al. (2020) are plotted on the same heliocentric distance (r) scale (open circles) for comparison.

utilizing apertures with radii of $5''$ (where the image pixel scale was $1''$ arcsec^{-1}). These data mostly consisted of single g'- or r'-band detections on each night but included pairs of g' and r'-band detections on 2025 May 22 and June 18. We compute inferred V-band absolute magnitude from these data assuming a standard asteroidal phase function (E. Bowell et al. 1989) assuming $G = 0.15$ and solar colors (J. Holmberg et al. 2006; K. Jordi et al. 2006). We use this to present a secular light curve in Figure 5. The computed absolute magnitudes are relatively constant between 2025 May 22 and June 14 (during which the object ranged between heliocentric distances of $r = 5.8$ and 5.1 au). The secular light curve has a median value of $H_V \sim 12.4$ and a standard deviation of ~ 0.1 mag. No uncertainties were reported for these ZTF data in MPEC 2025-N51. Therefore we adopt this standard deviation as an approximate uncertainty level for all ZTF photometry reported here for 3I/ATLAS based on the scatter in the available photometric points between 2025 May 22 and June 14.

Figure 5 also includes the corresponding H_V of 2I/Borisov's unresolved coma from prediscovery ZTF observations of that comet (Q. Ye et al. 2020) at similar r for comparison. If the 3I/ATLAS photometry is also measuring the brightness of an unresolved coma, the similarity of the two interstellar comets' H_V magnitudes at $r \simeq 5$–6 au preperihelion suggests that 3I/ATLAS may have a kilometer-scale nucleus comparable in size to that of 2I/Borisov, if the two nuclei are similar in composition or otherwise eject a comparable amount of dust per unit cross section under equivalent solar heating.

The photometry from 2025 June 18 (the last night plotted in Figure 5 when the object was at $r = 4.9$ au) corresponds to an absolute magnitude outside that standard deviation at $H_V = 12.1 \pm 0.1$. For comparison, r'-band light-curve data obtained from LCO network telescopes (discussed in more detail in Section 3.2) show an approximate average r'-band apparent magnitude of $m_r \sim 17.9$, corresponding to $H_V = 11.9$, indicating that the faint coma visible in CFHT and VLT data obtained on 2025 July 2 and 4 could be responsible for about 0.5 mag of excess brightening of the object since early June.

We note that this finding does not exclude the presence of coma prior to mid-June but indicates that any coma that may have been present was relatively steady-state from late May to early June and then increased in mid-June. For reference,

$H_V = 12.4 \pm 0.1$ corresponds to a radius of $\sim(10 \pm 1)$ km for a geometric albedo of $p_V = 0.05$ typical of comets, but this is an upper limit, given that the object was active during the observations used to derive this result.

3.2. Rotation

In order to characterize 3I/ATLAS's rotational light curve, we obtained time-series observations between 2025 July 2 and 4 using two separate 0.35 m telescopes from the LCO Haleakalā observatory (MPC codes T03, T04), the 2.0 m FTN (MPC code F65) at Haleakalā Observatory, and the 2.0 m FTS (MPC code E10) at Siding Spring Observatory, all of which are part of the same network. Time-series observations were also obtained on 2025 July 4–5 using the Telescope Joan Oró (TJO; MPC code C65) at Montsec Observatory.

Photometric observations of 3I/ATLAS were obtained on the nights of 2025 July 2–4 with the TRAPPIST telescopes (E. Jehin et al. 2011). TRAPPIST-North (TN; MPC code Z53) is located at the Oukaimeden observatory in Morocco, and TRAPPIST-South (TS; MPC code I40) is located at the ESO La Silla Observatory in Chile. Both telescopes are 0.6 m Ritchey–Chretien telescopes operating at f/8. The TN camera is an Andor IKONL BEX2 DD camera providing a $20'$ field of view and pixel scale of $1''20$ pixel^{-1} (using 2×2 binning). TS is equipped with an FLI ProLine 3041-BB CCD camera with a $22'$ field of view and a pixel scale of $1''28$ pixel^{-1} (using 2×2 binning). Johnson–Cousin R_c filters were used with individual exposure times of 180 s on both telescopes.

To compensate for the dense star fields in the TRAPPIST observations, an average template image constructed from 10 adjacent images is subtracted from each image in each set of data, where reference stars are used to compensate for extinction variations between science and template images. This results in far less background-source-contaminated data from which photometry of 3I/ATLAS can be measured. We then perform aperture photometry using PHOTOMETRYPIPELINE (M. Mommert 2017) by matching ~ 100 field stars in each image with the Pan-STARRS DR1 photometric catalog and using photometry aperture radii of 4 pixels ($4''8$ on TN and $5''1$ on TS).
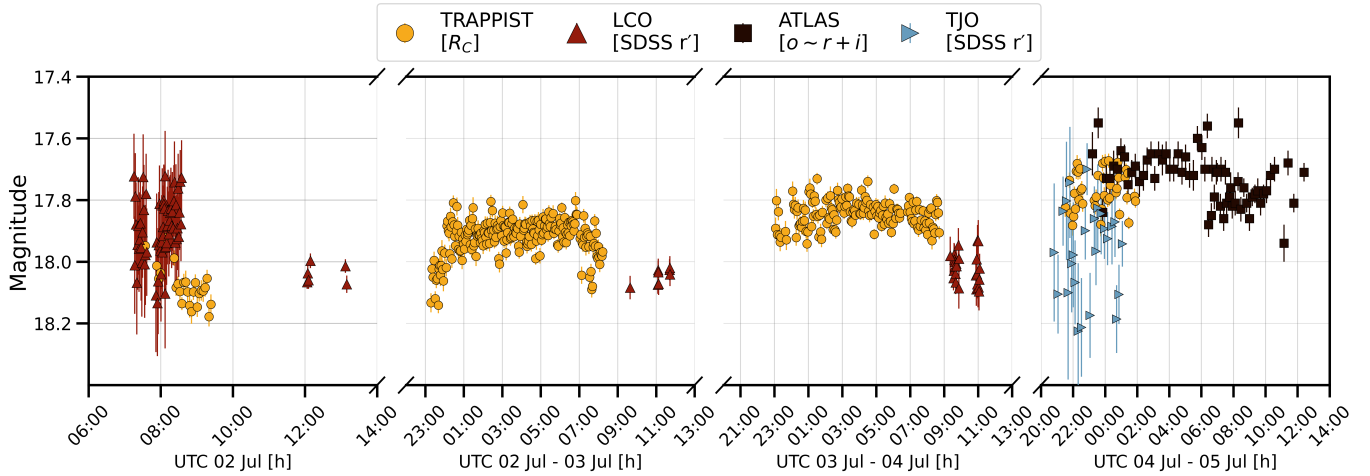
Figure 6. Compiled light curve of 3I/ATLAS incorporating r′-band data from the LCO 0.35 m telescopes, FTN, FTS, and the TJO, Johnson–Cousins R_c-band data from the TN and TS telescopes, and o-band data from ATLAS-HKO and ATLAS-CHL. A summary of parameters used in the measurement of these data is shown in Table 2. Tabular data for photometry plotted in this figure are available at https://3i-atlas.github.io/data.html.

Table 2
Light-curve Observations Summary

Facility/Instrument	MPC Site Code	Observation Dates (UT)	Filter(s)	Pixel Scale	Photometry Method	Aperture Radius[a]
ATLAS (Haleakala)	W68	2025 July 4	o	1″86	PSF	n/a
ATLAS (Chile)	T05	2025 July 4	o	1″86	PSF	n/a
FTN	F65	2025 July 2, 4	r′	0″28	aperture	2″2
FTS	E10	2025 July 2, 4	r′	0″28	aperture	2″2
LCO 0.35 m (Haleakalā #1)	T03	2025 July 2, 4	r′	0″74	aperture	3″0
LCO 0.35 m (Haleakalā #2)	T04	2025 July 2, 4	r′	0″74	aperture	3″0
TJO	C65	2025 July 4–5	r′	0″72	aperture	2″2
TN	Z53	2025 July 2–4	R_c	1″20	aperture	4″8
TS	I40	2025 July 2–4	R_c	1″28	aperture	5″1

Note.
[a] Photometry aperture size if aperture photometry is used; otherwise, this field is not applicable.

We also obtained time-series observations of 3I/ATLAS in o-band (AB; approximately equivalent to $r' + i'$) using the ATLAS network starting at ∼23:00 UTC on 2025 July 4. Using the ATLAS sites in Chile and Haleakalā (ATLAS-HKO and ATLAS-CHL; MPC codes W68 and T05), a 13 hr continuous light curve was obtained from the normal differencing pipeline. These photometric measurements were performed on difference images using PSF-based forced photometry (i.e., fitting a stellar PSF to the flux at the expected position of the target in each image and measuring the magnitude of the best-fit PSF, which, it should be noted, may underreport the brightness of extended sources like 3I/ATLAS) using PSFs derived from nearby field stars (J. L. Tonry et al. 2018a; K. W. Smith et al. 2020). The zero point for each exposure is derived from ∼10^5 reference stars from Refcat2 (J. L. Tonry et al. 2018b).

A summary of the facilities and photometry methods used to collect and measure these data is shown in Table 2. Compiled light-curve results are shown in Figure 6. In this plot, offsets between data sets may be attributed to different filters being used, differences between photometry measurement methods (i.e., PSF-based photometry for ATLAS data versus aperture

photometry for all other data sets), differences in apertures used for the data sets measured using aperture photometry, and changes in observing geometry as these data have not been corrected for changes in heliocentric and geocentric distance or solar phase angle.

No periodicity is immediately apparent within any of the data sets, indicating little brightness variation ≲0.2 mag during the observation period, where some scatter may also be due to background source contamination (or residual contamination in the cases of data for which image differencing has been applied). This is in notable contrast to 1I/'Oumuamua, which displayed a far more extreme light-curve range of ∼3.5 mag (see Section 1). It should be noted, however, that the detection of activity and coma (Section 3.1) means that any photometric variations caused by a rotating nucleus will be at least partially suppressed by the relatively more steady-state coma surrounding it. A more detailed analysis of these data will be presented in a future work, though we note that R. de la Fuente Marcos et al. (2025) reported a tentative periodicity in time-series observations, finding a period of 16.79 hr, minimum brightness at MJD 60861.00, and an amplitude 0.08 mag, which agrees well with our 14h ATLAS light curve.
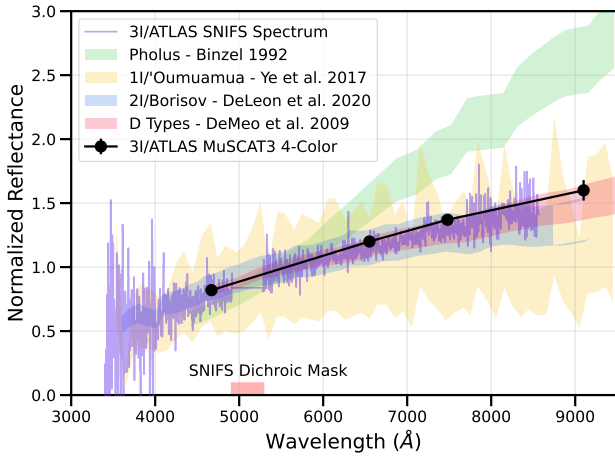
Figure 7. The g', r', i', z' colors of 3I/ATLAS obtained with FTN converted to a solar reflectivity as well as the reflectance spectrum obtained with SNIFS on the UH 2.2 m at Maunakea normalized at 5500 Å are plotted in comparison to 1I/'Oumuamua (Q.-Z. Ye et al. 2017), 2I/Borisov (J. de León et al. 2020), the extremely red Centaur Pholus (R. P. Binzel 1992), and the mean D-type asteroid spectrum (F. E. DeMeo et al. 2009). The errors on the FTN photometric data are approximately the size of the plot points. The region of the spectrum masked due to the SNIFS dichroic sensitivity is indicated in red. Both the observed spectrum and the four-color-derived reflectance slopes are in agreement. Moreover, 3I/ATLAS shows a moderately red spectral slope similar to 1I/'Oumuamua and 2I/Borisov.

3.3. Colors

Two multifilter imaging sequences were obtained with the 2.0 m FTN on Haleakalā using the four-channel MuSCAT3 imager, which records the Sloan g'-, r'-, i'-, and z_s-bands simultaneously: (i) six exposures of 30 s in each filter and (ii) three exposures of 50 s in each filter, yielding total integrations of 180 and 150 s per band, respectively. The data output by the LCO reduction pipelines were processed with PHOTOMETRY-PIPELINE (M. Mommert 2017), which performs SCAMP astrometric solutions against Gaia DR3 (Gaia Collaboration et al. 2023) and aperture photometry using apertures with radii of 1″46 (5.4 pixels) and calibrated to Pan-STARRS DR2 (H. A. Flewelling et al. 2020). From these data, we find mean colors of $g' - r' = 0.85 \pm 0.03$, $r' - i' = 0.25 \pm 0.03$, and $i' - z' = 0.20 \pm 0.08$.

In Figure 7, we show the resulting four-color surface reflectance spectrum of the object from the FTN. The colors of 3I/ATLAS, as seen in Figure 7, are relatively linear (e.g., without obvious absorption features or spectral curvature) and significantly redder than those of the Sun. This slope of this reflectance spectrum is approximately 18%/100 nm, as derived from the full range of the available color data. It is similar, though somewhat redder, to that retrieved for 1I/'Oumuamua ($10\% \pm 6\%/100$ nm, Q.-Z. Ye et al. 2017) and 2I/Borisov ($12\% \pm 1\%/100$ nm J. de León et al. 2020), both of which are slightly redder than the D-type asteroids (F. E. DeMeo et al. 2009). Moreover, it is within the range found for 1I/'Oumuamua of 7%–23%/100 nm reported by A. Fitzsimmons et al. (2018). However, it is not as red as seen in some outer solar system objects (e.g., Pholus, R. P. Binzel 1992). Some of the reflected light must be from the coma because 3I/ATLAS is weakly active. This is corroborated by the fact that photometry of g'- and r'-band ZTF precovery data (Section 3.1), obtained when the object appeared to be less active, indicated that the $g' - r'$ colors on those nights were close to solar (within large uncertainties).

Specifically, the measurements were $(g' - r'') = 0.42 \pm 0.14$ on 2025 May 22 and $(g' - r') = 0.44 \pm 0.14$ on June 18, compared to $(g' - r')_\odot = 0.45 \pm 0.02$ (J. Holmberg et al. 2006). This suggests that the much redder color measured from later data could be heavily affected by ejected dust. The spectral slope measured here is slightly higher than the average for cometary dust (see modeling and discussions of typical solar system comets in S. Protopapa et al. 2018; T. Kareta et al. 2023; Figure 3 of L. Kolokolova et al. 2024), but not significantly so. Moreover, 2I/Borisov's coma was similarly red (see, e.g., J. de León et al. 2020), but the object was also significantly more active at the time of the color observations.

3.4. Spectrum

The spectrum shown in Figure 7 was obtained on 2025 July 4 using the SuperNova Integral Field Spectrograph (SNIFS; B. Lantz et al. 2004) on the UH 2.2 m telescope at Maunakea by the Spectroscopic Classification of Astronomical Transients (SCAT; M. A. Tucker et al. 2022) team. Data reduction followed the procedures described in M. A. Tucker et al. (2022). SNIFS contains two channels split by a dichroic mirror, with a blue channel covering 0.34–0.51 μm and a red channel covering 0.51–1.0 μm, with spectral resolutions of 5 and 7 Å, respectively. The fast reduction pipeline used here does not include the full dichroic correction; therefore, data in this region were excluded from the final spectrum. In addition to 3I/ATLAS, the solar analog HD 165290 was observed. The final calibrated reflectance spectrum obtained by dividing the target spectrum by the normalized spectrum of the solar analog is shown in Figure 7.

The normalized reflection spectrum shows no obvious absorption features or gas emissions and yields a spectral slope of $17.1\% \pm 0.2\%/100$ nm measured from the spectrum window shown in Figure 7. This value was determined with a linear fitting routine with bootstrapping to estimate uncertainties. This spectral slope confirms the moderately red slope observed with the MuSCAT3 images, further solidifying a color similarity to both D-types and 2I/Borisov.

4. Discussion

Given that three interstellar objects have now been discovered, it is worthwhile to use their measured physical properties and discovery circumstances to estimate the size of the total population in the solar system.

The volume within which ATLAS can detect a moving object depends strongly on intrinsic brightness (H_V) and location in the solar system, where sensitivity, illumination, distance, phase function, and trailing losses are critical components. Using an ATLAS detection model that assumes a $G = 0.15$ phase function, a speed of 50 km s^{-1} for trailing losses, a weather and moon averaged limiting $m_{\mathrm{lim}} \simeq 19$, and 50 km s^{-1} speed for volume crossing, Figure 8 shows the volume in which ATLAS can detect an object.

This curve of detectability volume divided by crossing time has a slope of $\log(V/dt) \propto -0.2H_V$ for $H_V < 15$ and a slope of $\log(V/dt) \propto -0.4H_V$ for $H_V > 15$. However, the crossing time for $H > 16$ is less than 0.1 yr, which means that the actual detectability is certainly less than V/dt from Figure 8 because of weather and other survey cadence effects. The ratio of detectability volume and crossing time is approximately the product of detection cross section and velocity, hence the ratio
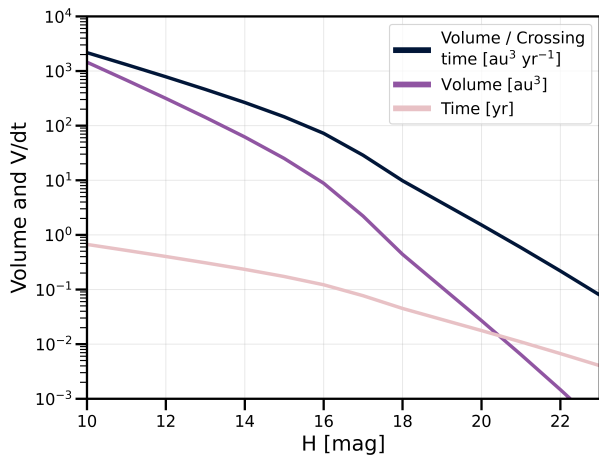
Figure 8. The volume in which ATLAS can detect an object is plotted as a function of H magnitude (red). The ratio of volume and crossing time (blue) is approximately the product of detection cross section and velocity. When the visibility time (green) becomes less than ∼0.1 yr (a lunation), weather and other effects will diminish the chances of a detection below the V/dt curve.

of detection rate and local density. Evaluating Figure 8 at $H_V \sim 12.5$ for 3I/ATLAS gives $600\,\mathrm{au^3\,yr^{-1}}$ and a local density of $\sim 3 \times 10^{-4}\,\mathrm{au^{-3}}$ for a detection rate of $\sim 0.2\,\mathrm{yr^{-1}}$. While this calculation assumes a slightly different magnitude than that measured for 3I/ATLAS, it is worth noting that H_V will likely change for 3I/ATLAS depending on whether the activity level changes. In this case since H_V of 3I/ATLAS was measured when active, this limiting search volume corresponds to the absolute brightness of the inert nucleus.

The $G = 0.15$ phase function used for Figure 8 may be inappropriate for an object such as 3I/ATLAS with an unknown amount of coma and unknown and potentially unfamiliar surface scattering properties, which could cause this density estimate to be significantly incorrect. Obtaining stronger constraints on 3I/ATLAS's nucleus size, such as with high-resolution imaging by space telescopes or adaptive optics-equipped ground-based telescopes, or by searching for occultation observation opportunities, should therefore be considered a high priority.

A. Do et al. (2018) estimated an interstellar density of objects like 1I/'Oumuamua at $0.2\,\mathrm{au^{-3}}$ ($H_V \sim 23$) and noted that the size distribution must be steeper than $n(d > D) \propto D^{-3}$ to avoid a logarithmic divergence in total mass, i.e., differential $\log n(d)$ with slope greater than $0.8 H_V$ (see Figure 3 of A. Do et al. 2018). This criterion applied to the ATLAS detectability curve would cause a strong peak around $H \sim 16$, not two detections at $H \sim 13$, however. As such, the detections of 2I/Borisov and 3I/ATLAS, both of which appear, or appeared, relatively large, are somewhat unexpected given that more numerous smaller interstellar objects have not also been discovered over the same time period. Clearly what is needed is more interstellar object discoveries to improve population statistics, which is hopefully exactly what the Rubin Observatory Legacy Survey of Space and Time (R. L. Jones et al. 2009) will deliver in the coming years.

We are certain to learn more about 3I/ATLAS in the coming weeks and months as it experiences continued and increasing heating for perhaps the first time during its passage past our Sun. Comprehensive and collaborative investigations of 3I/ATLAS based off the lessons learned from the 1I/ 'Oumuamua and 2I/Borisov campaigns are poised to

significantly expand our knowledge of the interstellar object population, and as such, additional observations of 3I/ATLAS are highly encouraged. Further photometry, spectroscopy, or polarimetry could constrain the rotation, activity, dust size–frequency distribution, coma composition, and nongravitational acceleration of the object. The perihelion of 3I/ATLAS will not be easily observable from Earth-based observatories as the object will be on the opposite side of the Sun and at a low solar elongation angle. However, the object will approach within 0.19 au of Mars, and we encourage nearby spacecraft (e.g., Mars Reconnaissance Orbiter, Trace Gas Orbiter, MAVEN, Tianwen-1, Hope, and Jupiter Icy Moons Explorer) equipped with visible, UV, and IR spectrographs and cameras to attempt to capture data on this object's closest approach.

Author Contributions

D.Z.S. led the manuscript writing and figure generation and coordinated observations.

M.M. contributed the initial orbital assessment work, wrote part of the manuscript, extracted high-precision astrometry from the observations of the team, and, together with D.F., M.F., and L.F., provided orbit fitting and ephemeris calculations for follow-up observations.

J.T., L.D., and others built and operate the system (ATLAS) that discovered the object. J.T. and L.D. obtained and measured the 14 hr follow-up light curve and contributed to the manuscript. J.T. calculated ATLAS detection cross sections and provided a discussion about rates and densities.

A.H. helped with data reduction and contributed to the manuscript review.

M.D., T.S.-R., and M.M. obtained the color data at LCO, reduced the data, produced the color spectrum, and contributed to the manuscript.

E.J., M. F., M.A.M, J.M., and M.G. observed 3I for several nights with both TRAPPIST telescopes, reduced and measured the data to obtain light curves, and contributed to the manuscript.

E.P.-A. contributed to figure generation and manuscript review.

H.H.H. contributed to figure generation, analyzed ZTF precovery data, and reviewed and contributed to the manuscript.

J.V.K. and J.J.W. contributed to and reviewed the manuscript.

J.W.N. contributed to figure generation, consolidated light-curve data sets, and reviewed and contributed to the manuscript.

K.J.M. helped coordinate observations, worked to secure the VLT observing time, helped analyze the spectrum, and contributed to the manuscript.

O.R.H. was the PI on the VLT DDT proposal, executed the observations, produced the composite star stack, and contributed to the manuscript.

Q.Y. identified and measured the ZTF precovery data and contributed to the manuscript.

R.W. and R.W. obtained and measured CFHT data to search for cometary activity and contributed to and reviewed the manuscript.

F.O. and M.M. obtained the first astrometric tracklet by our team from ESA's TBT telescope.

A.D.F contributed to figure generation and manuscript review.

T.F., L.C., L.F., M.F., A.H., T.K., K.M., D.M., R.J.S., A.G.T., A.Y., B.Y., and Q.Z. contributed to the manuscript review.

T.L., C.E.H., and M.S.P.K. obtained and measured additional LCO data to confirm the orbit and analyze the light curve and contributed to the manuscript review.

T.S.-R. and M.D. obtained and measured the LCO and TJO data to study the light curve.
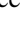
W.B.H., M.E.H., B.J.S., K.H., K.A., and M.A.T. are either Principal Investigators of the SCAT survey and/or obtained and reduced the SNIFS spectrum and reviewed the manuscript.

Data and Software Availability

The data behind many of the figures in this work are available at https://3i-atlas.github.io/data.html.

ORCID iDs

Darryl Z. Seligman ◉ https://orcid.org/0000-0002-0726-6480
Marco Micheli ◉ https://orcid.org/0000-0001-7895-8209
Davide Farnocchia ◉ https://orcid.org/0000-0003-0774-884X
Larry Denneau ◉ https://orcid.org/0000-0002-7034-148X
John W. Noonan ◉ https://orcid.org/0000-0003-2152-6987
Henry H. Hsieh ◉ https://orcid.org/0000-0001-7225-9271
Toni Santana-Ros ◉ https://orcid.org/0000-0002-0143-9440
John Tonry ◉ https://orcid.org/0000-0003-2858-9657
Katie Auchettl ◉ https://orcid.org/0000-0002-4449-9152
Luca Conversi ◉ https://orcid.org/0000-0002-6710-8476

Maxime Devogèle ⬤ https://orcid.org/0000-0002-6509-6360
Laura Faggioli ⬤ https://orcid.org/0000-0002-5447-432X
Adina D. Feinstein ⬤ https://orcid.org/0000-0002-9464-8101
Marco Fenucci ⬤ https://orcid.org/0000-0002-7058-0413
Marin Ferrais ⬤ https://orcid.org/0000-0002-0535-652X
Tessa Frincke ⬤ https://orcid.org/0009-0000-4697-5450
Michael Gillon ⬤ https://orcid.org/0000-0003-1462-7739
Olivier R. Hainaut ⬤ https://orcid.org/0000-0001-6952-9349
Kyle Hart ⬤ https://orcid.org/0009-0003-2390-2840
Andrew Hoffman ⬤ https://orcid.org/0000-0002-8732-6980
Carrie E. Holt ⬤ https://orcid.org/0000-0002-4043-6445
Willem B. Hoogendam ⬤ https://orcid.org/0000-0003-3953-9532
Mark E. Huber ⬤ https://orcid.org/0000-0003-1059-9603
Emmanuel Jehin ⬤ https://orcid.org/0000-0001-8923-488X
Theodore Kareta ⬤ https://orcid.org/0000-0003-1008-7499
Jacqueline V. Keane ⬤ https://orcid.org/0000-0002-2021-1863
Michael S. P. Kelley ⬤ https://orcid.org/0000-0002-6702-7676
Tim Lister ⬤ https://orcid.org/0000-0002-3818-7769
Kathleen Mandt ⬤ https://orcid.org/0000-0001-8397-3315
Jean Manfroid ⬤ https://orcid.org/0000-0002-6930-2205
Dušan Marčeta ⬤ https://orcid.org/0000-0003-4706-4602
Karen J. Meech ⬤ https://orcid.org/0000-0002-2058-5670
Mohamed Amine Miftah ⬤ https://orcid.org/0009-0003-1220-6532
Marvin Morgan ⬤ https://orcid.org/0000-0003-4022-6234
Francisco Ocaña ⬤ https://orcid.org/0000-0002-9836-3285
Eloy Peña-Asensio ⬤ https://orcid.org/0000-0002-7257-2150
Benjamin J. Shappee ⬤ https://orcid.org/0000-0003-4631-1149
Robert J. Siverd ⬤ https://orcid.org/0000-0001-5016-3359
Aster G. Taylor ⬤ https://orcid.org/0000-0002-0140-4475
Michael A. Tucker ⬤ https://orcid.org/0000-0002-2471-8442
Richard Wainscoat ⬤ https://orcid.org/0000-0002-1341-0952
Robert Weryk ⬤ https://orcid.org/0000-0002-0439-9341
James J. Wray ⬤ https://orcid.org/0000-0001-5559-2179
Atsuhiro Yaginuma ⬤ https://orcid.org/0009-0001-9538-1971
Bin Yang ⬤ https://orcid.org/0000-0002-5033-9593
Quanzhi Ye
(叶泉志) ⬤ https://orcid.org/0000-0002-4838-7676
Qicheng Zhang ⬤ https://orcid.org/0000-0002-6702-191X

References

Alarcon, M. R., Serra-Ricart, M., Licandro, J., et al. 2025, ATel, 17264, 1A
Almeida-Fernandes, F., & Rocha-Pinto, H. J. 2018, MNRAS, 480, 4903
Aravind, K., Ganesh, S., Venkataramani, K., et al. 2021, MNRAS, 502, 3491
Bagnulo, S., Cellino, A., Kolokolova, L., et al. 2021, NatCo, 12, 1797
Bannister, M. T., Opitom, C., Fitzsimmons, A., et al. 2020, arXiv:2001.11605
Bellm, E. C., Kulkarni, S. R., Graham, M. J., et al. 2019, PASP, 131, 018002
Belton, M. J. S., Hainaut, O. R., Meech, K. J., et al. 2018, ApJL, 856, L21
Belyakov, M., Fremling, C., Graham, M. J., et al. 2025, RNAAS, 9, 194
Bergner, J. B., & Seligman, D. Z. 2023, Natur, 615, 610
Binzel, R. P. 1992, Icar, 99, 238
Biver, N., Dello Russo, N., Opitom, C., & Rubin, M. 2024, in Comets III, ed. K. J. Meech et al. (University of Arizona Press), 459
Bodewits, D., Noonan, J. W., Feldman, P. D., et al. 2020, NatAs, 4, 867
Borisov, G., Durig, D. T., Sato, H., et al. 2019, Comet C/2019 Q4 (Borisov), Central Bureau Electronic Telegrams, 4666, 1
Boulade, O., Charlot, X., Abbon, P., et al. 2003, Proc. SPIE, 4841, 72
Bowell, E., Hapke, B., Domingue, D., et al. 1989, in Asteroids II (Tucson, AZ: Univ. of Arizona Press), 524
Cordiner, M. A., Milam, S. N., Biver, N., et al. 2020, NatAs, 4, 861
Cremonese, G., Fulle, M., Cambianica, P., et al. 2020, ApJL, 893, L12
de la Fuente Marcos, R., Licandro, J., Alarcon, M. R., et al. 2025, arXiv:2507.12922
de León, J., Licandro, J., de la Fuente Marcos, C., et al. 2020, MNRAS, 495, 2053
DeMeo, F. E., Binzel, R. P., Slivan, S. M., & Bus, S. J. 2009, Icar, 202, 160
Denneau, L., Siverd, R., Tonry, J., et al. 2025, MPEC, N, 12
Desch, S. J., & Jackson, A. P. 2021, JGRE, 126, e2020JE006807
Desch, S. J., & Jackson, A. P. 2022, AsBio, 22, 1400
Do, A., Tucker, M. A., & Tonry, J. 2018, ApJL, 855, L10
Farnocchia, D., Seligman, D. Z., Granvik, M., et al. 2023, PSJ, 4, 29
Feng, F., & Jones, H. R. A. 2018, ApJL, 852, L27
Fitzsimmons, A., Hainaut, O., Meech, K. J., et al. 2019, ApJL, 885, L9
Fitzsimmons, A., Meech, K., Matrà, L., & Pfalzner, S. 2024, in Comets III, ed. K. J. Meech et al. (Tucson, AZ: Univ. of Arizona Press), 731
Fitzsimmons, A., Snodgrass, C., Rozitis, B., et al. 2018, NatAs, 2, 133
Flekkøy, E. G., Luu, J., & Toussaint, R. 2019, ApJL, 885, L41
Flewelling, H. A., Magnier, E. A., Chambers, K. C., et al. 2020, ApJS, 251, 7
Fraser, W. C., Pravec, P., Fitzsimmons, A., et al. 2018, NatAs, 2, 383
Gaia Collaboration, Vallenari, A., Brown, A. G. A., et al. 2023, A&A, 674, A1
Gaidos, E., Williams, J., & Kraus, A. 2017, RNAAS, 1, 13
Graham, M. J., Kulkarni, S. R., Bellm, E. C., et al. 2019, PASP, 131, 078001
Guzik, P., Drahus, M., Rusek, K., et al. 2020, NatAs, 4, 53
Hallatt, T., & Wiegert, P. 2020, AJ, 159, 147
Hibberd, A., Crowl, A., & Loeb, A. 2025, arXiv:2507.12213
Holmberg, J., Flynn, C., & Portinari, L. 2006, MNRAS, 367, 449
Hopkins, M. J., Dorsey, R. C., Forbes, J. C., et al. 2025, arXiv:2507.05318
Hsieh, C.-H., Laughlin, G., & Arce, H. G. 2021, ApJ, 917, 20
Hui, M.-T., Ye, Q.-Z., Föhring, D., Hung, D., & Tholen, D. J. 2020, AJ, 160, 92
Jackson, A. P., & Desch, S. J. 2021, JGRE, 126, e2020JE006706
Jehin, E., Gillon, M., Queloz, D., et al. 2011, Msngr, 145, 2
Jewitt, D., & Luu, J. 2019, ApJL, 886, L29
Jewitt, D., & Luu, J. 2025, ATel, 17263, 1J
Jewitt, D., Luu, J., Rajagopal, J., et al. 2017, ApJL, 850, L36
Jewitt, D., & Seligman, D. Z. 2023, ARA&A, 61, 197
Jones, R. L., Chesley, S. R., Connolly, A. J., et al. 2009, EM&P, 105, 101
Jordi, K., Grebel, E. K., & Ammon, K. 2006, A&A, 460, 339
Kareta, T., Noonan, J. W., Harris, W. M., & Springmann, A. 2023, PSJ, 4, 85
Kareta, T., Andrews, J., Noonan, J. W., et al. 2020, ApJL, 889, L38
Kareta, T., Champagne, C., McClure, L., et al. 2025, arXiv:2507.12234
Kim, Y., Jewitt, D., Mutchler, M., et al. 2020, ApJL, 895, L34
Knight, M. M., Protopapa, S., Kelley, M. S. P., et al. 2017, ApJL, 851, L31
Kolokolova, L., Kelley, M. S. P., Kimura, H., & Hoang, T. 2024, in Comets III, ed. K. J. Meech et al. (Tucson, AZ: Univ. of Arizona Press), 621
Lantz, B., Aldering, G., Antilogus, P., et al. 2004, Proc. SPIE, 5249, 146
Levine, W. G., Cabot, S. H. C., Seligman, D., & Laughlin, G. 2021, ApJ, 922, 39
Levine, W. G., & Laughlin, G. 2021, ApJ, 912, 3
Lin, H. W., Lee, C.-H., Gerdes, D. W., et al. 2020, ApJL, 889, L30
Lister, T., Kelley, M. S. P., Holt, C. E., et al. 2022, PSJ, 3, 173
Loeb, A. 2025, arXiv:2507.05881
Luu, J. X., Flekkøy, E. G., & Toussaint, R. 2020, ApJL, 900, L22
Mamajek, E. 2017, RNAAS, 1, 21
Mashchenko, S. 2019, MNRAS, 489, 3003
McKay, A. J., Cochran, A. L., Dello Russo, N., & DiSanti, M. A. 2020, ApJL, 889, L10
Meech, K. J., Weryk, R., Micheli, M., et al. 2017, Natur, 552, 378
Micheli, M., Farnocchia, D., Meech, K. J., et al. 2018, Natur, 559, 223
Mommert, M. 2017, A&C, 18, 47
Moro-Martín, A. 2019, ApJL, 872, L32
Moro-Martín, A. 2022, arXiv:2205.04277
Opitom, C., Fitzsimmons, A., Jehin, E., et al. 2019, A&A, 631, L8
Opitom, C., Snodgrass, C., Jehin, E., et al. 2025, arXiv:2507.05226
Protopapa, S., Kelley, M. S. P., Yang, B., et al. 2018, ApJL, 862, L16
Sekanina, Z. 2019, arXiv:1905.00935
Seligman, D., & Laughlin, G. 2020, ApJL, 896, L8
Seligman, D. Z., Farnocchia, D., Micheli, M., et al. 2023, PSJ, 4, 35
Seligman, D. Z., Farnocchia, D., Micheli, M., et al. 2024, PNAS, 121, e2406424121
Seligman, D. Z., & Moro-Martín, A. 2023, ConPh, 63, 200
Smith, K. W., Smartt, S. J., Young, D. R., et al. 2020, PASP, 132, 085002
Taylor, A. G., & Seligman, D. Z. 2025, arXiv:2507.08111
Taylor, A. G., Seligman, D. Z., Hainaut, O. R., & Meech, K. J. 2023, PSJ, 4, 186
Taylor, A. G., Steckloff, J. K., Seligman, D. Z., et al. 2024, Icar, 420, 116207

Tonry, J. L., Denneau, L., Flewelling, H., et al. 2018b, ApJ, 867, 105
Tonry, J. L., Denneau, L., Heinze, A. N., et al. 2018a, PASP, 130, 064505
Trilling, D. E., Mommert, M., Hora, J. L., et al. 2018, AJ, 156, 261
Tucker, M. A., Shappee, B. J., Huber, M. E., et al. 2022, PASP, 134 124502
Williams, G. V., Sato, H., Sarneczky, K., et al. 2017, Minor Planets 2017 SN_33 and 2017 U1, Central Bureau Electronic Telegrams, 4450, 1

Xing, Z., Bodewits, D., Noonan, J., & Bannister, M. T. 2020, ApJL, 893, L48
Yaginuma, A., Frincke, T., Seligman, D. Z., et al. 2025, arXiv:2507.15755
Yang, B., Meech, K. J., Connelley, M., & Keane, J. V. 2025, arXiv:2507. 14916
Yang, B., Li, A., Cordiner, M. A., et al. 2021, NatAs, 5, 586
Ye, Q., Kelley, M. S. P., Bolin, B. T., et al. 2020, AJ, 159, 77
Ye, Q.-Z., Zhang, Q., Kelley, M. S. P., & Brown, P. G. 2017, ApJL, 851, L5